Journal of Materials Chemistry C

PAPER

View Article Online
View Journal | View Issue

Cite this: J. Mater. Chem. C, 2017, 5, 9181

Two-dimensional hexagonal M_3C_2 (M = Zn, Cd and Hg) monolayers: novel quantum spin Hall insulators and Dirac cone materials†

Peng-Fei Liu,[abc] Liujiang Zhou,*[d] Sergei Tretiak[d] and Li-Ming Wu*[a]

Received 20th June 2017,
Accepted 15th August 2017

DOI: 10.1039/c7tc02739g

rsc.li/materials-c

The intriguing Dirac cones in honeycomb graphene have motivated the search for novel two-dimensional (2D) Dirac materials. Based on density functional theory and the global particle-swarm optimization method, herein, we predict a new family of 2D materials in honeycomb transition-metal carbides M_3C_2 (M = Zn, Cd and Hg) with intrinsic Dirac cones. The M_3C_2 monolayer is a kinetically stable state with a linear geometry (C═M═C), which to date has not been observed in other transition-metal-based 2D materials. The intrinsic Dirac cones in the Zn_3C_2, Cd_3C_2 and Hg_3C_2 monolayers arise from p–d band hybridizations. Importantly, the Hg_3C_2 monolayer is a room-temperature 2D topological insulator with a sizable energy gap of 44.3 meV. When an external strain is applied, additional phases with node-line semimetal states emerge in the M_3C_2 monolayer. These novel stable transition-metal–carbon-framework materials hold great promise for 2D electronic device applications.

Introduction

Two-dimensional (2D) topological insulators (TIs), also known as quantum spin Hall (QSH) insulators, constitute a remarkable class of atomically thin layered materials, which feature unique symmetry-protected metallic edge states sheltered from back-scattering. These are innovating functional materials due to their potential applications in dissipationless electronic devices.[1–5] Since the first 2D TI was proposed in graphene[2] by Kane and Mele, intensive efforts have been devoted to searching for new TIs in 2D crystals. This yielded a host of 2D TIs in p-block metal based 2D materials, such as silicene,[6,7] germanene,[8] stanene,[9] Bi_2Se_3,[10] 2D III-Bi compounds,[11] $BiCH_3$,[12] $GeCH_3$,[13] X2-GeSn,[14] GeI,[15] decorated stanene,[16] Bi_4F_4,[17] Bi_4Br_4,[18] BiX/SbX,[19] and GaBiCl.[20] Many of these systems are now considered for applications in future high-speed electronic-devices. However, the QSH effect, which is the prominent feature of 2D TIs, has only been experimentally realized in HgTe/CdTe[21] and InAs/GaSb[22] quantum wells. Recently, 2D transition-metal-based QSH insulators with large band gaps have also attracted great interest due to their high structural stability and diversity as well as strong resistance against thermal fluctuations at room temperature. These newly discovered 2D transition-metal-based TIs (*e.g.*, ZrC,[23] $ZrTe_5$,[24] MX (M = Zr and Hf; X = Cl, Br and I),[25] TaCX,[26] $Mo_2TiC_2O_2$,[27,28] MoC_6,[29] Cu_2Te,[30] HgSe,[31] 1T′-MoS_2,[32,33] so-MoS_2,[34–37] g-MoS_2,[38,39] 1T″-MoS_2,[40] TiNI[41] and g-MoN_2H_2[42]) greatly enrich the family of QSH insulators for practical applications. Importantly, 2D $ZrTe_5$ crystals have been already verified experimentally to possess an intrinsic QSH effect,[43,44] thus further confirming the potential of 2D transition-metal materials as topological insulators.

Amongst all the predicted and synthesized 2D crystals, the hexagonal lattice is the most favourable for 2D topological insulators with intrinsic massless Dirac fermions.[45] However, only several varieties of 2D TIs, which were predicted theoretically, are hexagonal lattices with intrinsic Dirac cones, including graphene,[1,2] silicene,[6,7] germanene,[8] and graphynes.[46,47] Recently, Liu and co-workers suggested the existence of intrinsic Dirac cones in transition-metal-based organic TIs by assembling molecular building blocks into a hexagonal lattice.[48,49] Compared to the well-known inorganic TIs, these transition-metal-based organic TIs greatly broaden the diversity of topological materials despite their tiny band gaps. However, these materials exhibit kinetic instability and pronounced imaginary frequencies in their phonon density of states,[50] which hamper the feasibility of experimental realization.

Inspired by previous studies, herein, our computational investigation predicts a novel family of 2D crystals in transition metal carbides M_3C_2 (M = Zn, Cd and Hg) with hexagonal

[a] State Key Laboratory of Structural Chemistry, Fujian Institute of Research on the Structure of Matter, Chinese Academy of Sciences, Fuzhou, Fujian 350002, People's Republic of China
[b] Institute of High Energy Physics, Chinese Academy of Sciences (CAS), Beijing 100049, China
[c] Dongguan Neutron Science Center, Dongguan 523803, China
[d] Theoretical Division, Center for Nonlinear Studies and Center for Integrated Nanotechnologies, Los Alamos National Laboratory, Los Alamos, New Mexico 87545, USA. E-mail: liujiang86@gmail.com, ljzhou86@lanl.gov

† Electronic supplementary information (ESI) available. See DOI: 10.1039/c7tc02739g

lattices, which favour a novel linear geometry (C═M═C). Our computations utilize the global particle swarm optimization (PSO) methodology[51] and density functional theory (DFT) methods.[52] In particular, we find that the M_3C_2 monolayer demonstrates a zero-gap semi-metal feature and possesses distinct Dirac cones in the absence of SOC, showing strong robustness against external strain. Remarkably, the Hg_3C_2 monolayer exhibits the QSH effect with an energy gap of 44 meV. Here, existence of topological helical edge states is rationalized by p–d band inversion, which is a distinguishing feature from other conventional TIs.

Methods

First-principles calculations were performed with the Vienna ab initio simulation package (VASP)[52] within the framework of the Perdew–Burke–Ernzerhof (PBE)[53] generalized gradient approximation (GGA),[54] and plane-wave basis sets of 500 eV on the 0.01 $Å^{-1}$ spacing Monkhorst–Pack mesh. A slab model, together with a vacuum layer larger than 15 Å, was employed in all calculations. Geometries were fully relaxed until the residual forces on each atom became less than 0.01 eV $Å^{-1}$. The dynamic stabilities of all systems were checked by phonon calculations *via* the force-constant method[55] as implemented in the PHONOPY code.[56] Thermal stability was also examined *via* several *ab initio* molecular dynamics (AIMD) using the Nosé algorithm[57] in the *NVT* ensemble at the temperature of 1000 and 2000 K. To calculate the edge states of the Hg_3C_2 monolayer, the iterative Green's function[58] was firstly constructed *via* a tight-binding Hamiltonian in the basis of the maximally localized Wannier functions (MLWFs)[59] and then the edge states were computed from the imaginary part of the surface Green's function, as provided by WannierTools.[60]

Results and discussion

Our 2D metal carbide M_3C_2 (M = Zn, Cd and Hg) models were obtained from a global structure search as implemented in the CALYPSO code.[51] They adapt the hexagonal space group *P6/mmm* (No. 191) with $a = b$ = 6.52, 7.21, and 7.13 Å for Zn_3C_2, Cd_3C_2, and Hg_3C_2, respectively (Table 1). As shown in Fig. 1a, the 2D M_3C_2 are structurally analogous to the graphene-like Mg_3N_2 monolayer[61] with one unique metal atom (site symmetry 3g) and one independent C atom (site symmetry 2d) in the primitive unit. All C atoms are trigonally coordinated to ambient M atoms *via* sp^2-hybridization. The structure can be viewed as an enlarged graphene framework with metal atoms linearly inserted in between 2 C atoms, which favours strong extended π bonds and stabilizes the 2D sheets.[61]

Table 1 Calculated lattice parameters [lattice constants (l_a) and bond lengths of M–N bonds], cohesive energies (E_{coh}), topological Z_2 invariant and band gaps with and without SOC for the M_3C_2 sheets

Comp.	l_a (Å)	l_{M-N} (Å)	E_{coh} (eV)	PBE	PBE + SOC (meV)	HSE + SOC (meV)	Z_2
Zn_3C_2	6.52	1.88	2.52	sm[a]	1.2	1.1	1
Cd_3C_2	7.21	2.08	1.97	sm[a]	4.7	3.8	1
Hg_3C_2	7.13	2.06	1.79	sm[a]	44.3	37.4	1

[a] Semi-metal.

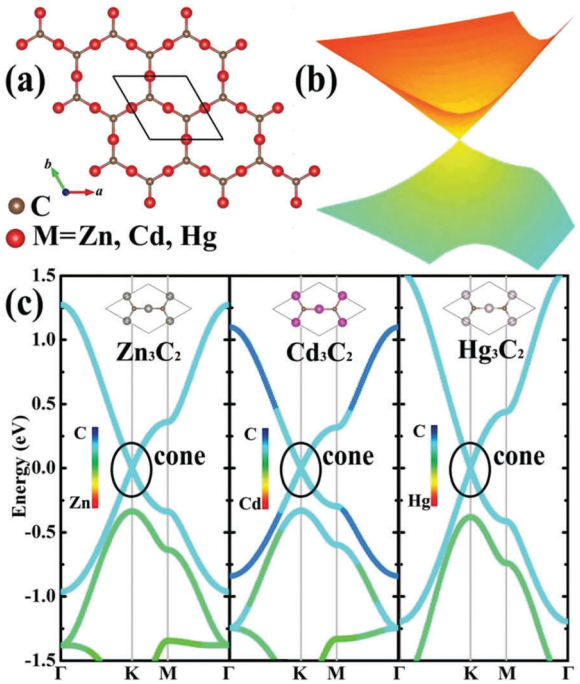

Fig. 1 (a) Top view of the M_3C_2 monolayer. Primitive unit cells are emphasized by the solid black line. (b) 3D projection of the Dirac cone of the Cd_3C_2 monolayer in the vicinity of the *K* point. (c) Orbital-resolved band structures for the M_3C_2 monolayers. The Fermi level is set to zero.

To evaluate the stability of the M_3C_2 lattice, we first computed the cohesive energy[61] with respect to the isolated atoms, which is defined as $E_{coh} = (3E_M + 2E_C - E_{2D})/5$, where E_{2D} is the total energy of the monolayer, and E_M and E_C are the energies of a single metal atom and a C atom, respectively. Our results show that the Zn_3C_2, Cd_3C_2 and Hg_3C_2 monolayers have cohesive energies of 2.52, 1.97, and 1.79 eV per atom, respectively. The obtained values are lower than that of graphene (7.85 eV per atom), silicene (3.91 eV per atom),[6,7] germanene (3.34 eV per atom),[8] stanene (3.03 eV per atom),[9] phosphorene (3.48 eV per atom),[62,63] but comparable with grey arsenene (2.40 eV per atom),[64,65] greyantimonene (2.30 eV per atom),[64,65] and metallic bismuthene (2.26 eV per atom).[64,65] This implies that the M_3C_2 sheet might be synthesized by epitaxial growth on an appropriate substrate such as silicone.[66]

The phonon spectrum and projected phonon density of states shown in Fig. S1 (ESI†) were calculated to check the dynamical stability of the M_3C_2 monolayer. All branches over the entire Brillouin zone are appreciably positive phonon vibrational modes, which indicate that the M_3C_2 monolayer is at the energy minimum. From the projected phonon density of states, it can be seen that the phonon spectrum mainly contains the out-plane vibrations in the low-energy region, especially at the zero point, whereas the contributions from in-plane vibrations become larger when going from the 0 THz

to 15 THz energy region. The high-energy regions are dominated solely by the in-plane vibrations, suggesting that the contributions mainly stem from the strong π-conjugated bonds which potentially further stabilize the planar geometry.

The mechanical stability of the M_3C_2 monolayer can also be assessed *via* elastic constants. The calculated 2D linear elastic constants are C_{11} = 39.71, 31.74 and 41.16 N m^{-1} and C_{12} = 34.46, 26.84, and 33.41 N m^{-1} for the Zn_3C_2, Cd_3C_2 and Hg_3C_2 monolayers, respectively. These values are significantly smaller than that of graphene (C_{11} = 358.1 N m^{-1} and C_{12} = 60.4 N m^{-1})[67] and fall under the Born criteria,[68] which further confirm their mechanically stability.

We next examined the thermal stability of the M_3C_2 monolayers by carrying out AIMD simulations. As shown in Fig. S2 (ESI†), the M_3C_2 monolayers at 1000 K do not undergo drastic structural distortions or transformations and can be optimized back to their initial structures *via* simple relaxation calculations. However, the snapshots of the Cd_3C_2 and Hg_3C_2 monolayers at 2000 K show the significant distortions of the geometry. Thus the M_3C_2 monolayers are all thermally stable at least up to 1000 K.

To study the electronic properties of the M_3C_2 monolayer, we next calculated their band structures as, shown in Fig. 1 and 2. The monolayer is a zero-band-gap semi-metal with the valence band (VB) and conduction band (CB) touching each other at the *K* point in the absence of SOC (Fig. 1). It can be seen that linear band dispersion appears around the Fermi level, which creates the intrinsic Dirac cone (Fig. 1b). When SOC is taken into account, the Dirac cones are well retained for Zn_3C_2 and Cd_3C_2 with enlarged band gaps of 1.2 and 4.7 meV at the Dirac points, respectively, which indicate the robustness of the Dirac cones against SOC. This feature renders Zn_3C_2 and Cd_3C_2 as 2D Dirac cone materials with negligible energy gaps. For the Hg_3C_2 monolayer, SOC introduces a larger gap of 44.3 meV in the massless Dirac fermion (Fig. 2), which gives rise to room-temperature topological insulating states. Refined calculations based on the Heyd–Scuseria–Ernzerhof (HSE06) hybrid functional[69,70] give band gaps of 1.1, 3.8 and 37.4 meV for the Zn_3C_2, Cd_3C_2 and Hg_3C_2 monolayers, respectively. Considering the point group symmetry (D_{6h}) for the Hg_3C_2 monolayer, the Hg-d orbitals are classified into three categories: d_{xy,x^2-y^2}, $d_{xz,yz}$, and d_{z^2}. In the vicinity of the Fermi level, the VB and CB mainly originate from the C p_z orbitals and some contributions from Hg-$p_{x,y}$, -d_{xy,x^2-y^2} orbitals (Fig. 2). Meanwhile, the VB-1 is primarily derived from the C-$p_{x,y}$ and Hg-$p_{x,y}$, -d_{xy,x^2-y^2} orbitals. Consequently, the $p_{x,y}$ and d_{xy,x^2-y^2} orbitals are responsible for the σ bonds, whereas the p_z, and $d_{xz,yz}$ orbitals are hybridized into π bonds, which yield the Dirac cones (Fig. 2 and Fig. S3, ESI†). Noticeably, such 2D π-conjugated local network owing to p–d hybridization leads to the linear geometry around the M atom bonding to two C atoms, which is to some extent analogous to the well-known d^{10} transition metals-based molecules such as CuI, AgI and AuI linearly coordinated with a ligand $[N{\equiv}C{-}M{-}C{\equiv}N]^-$.[71] Notably, such structure is yet to be observed in other 2D transition-metal-based crystals, which would advance the boundaries of coordination chemistry.

In order to gain more insight into the Dirac cone behaviour of the M_3C_2 sheet, we took the Hg_3C_2 monolayer as an example. Fig. 3 displays the difference charge density, the electron localization function (ELF)[72] and the partial charge densities at the Dirac points for this material. The plots reveal an electron abundant C-domain and electron deficient Hg atoms. The electrons are mainly localized at the strong Hg–C bonding regions. The ELF shows that there are high electron localization regions between the metal and carbon atoms. This indicates that the metal atoms serve as "–C≡C–" bonding structures in graphynes,[46] which bridge the gap between two C atoms[1] (Fig. 3a and b). In real space, the partial charge densities of the VB maximum (Fig. 3c) and CB minimum (Fig. 3d) confirm participation of the Hg-p_z, -$d_{xz,yz}$ and C p_z orbitals in the formation of Dirac cones, which further stabilizes the 2D frame structures of Hg_3C_2.

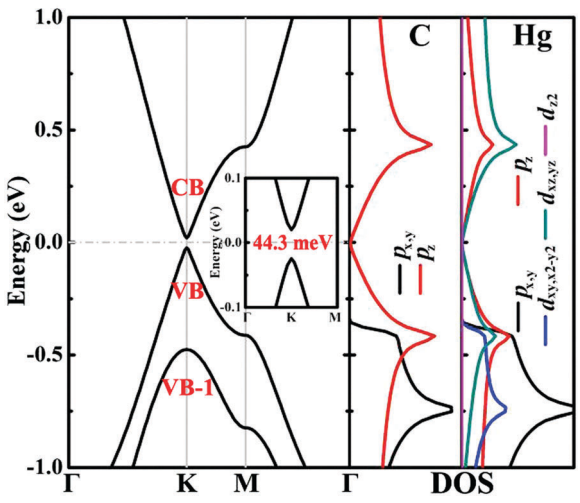

Fig. 2 Calculated band structures and projected density of states of the Hg_3C_2 monolayer with SOC. The Fermi level is set to zero.

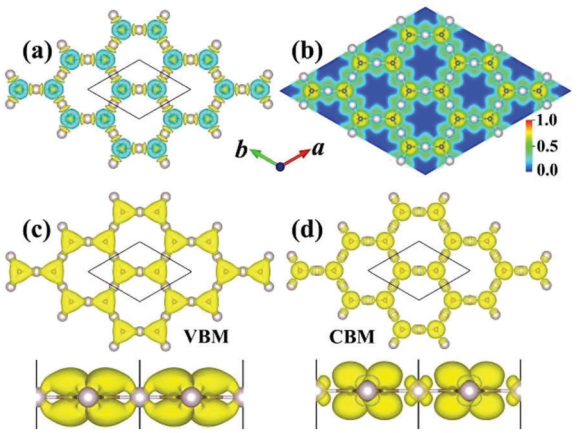

Fig. 3 (a) Difference charge density (isovalue: 0.07 e Å^{-3}; green: electron accumulation region; and yellow: electron depletion region.) and (b) electron localization function (ELF) of the Hg_3C_2 monolayer with an isovalue of 0.75 e Å^{-3}. Top and side views of (c) VB maximum and (d) CB minimum charge density contours at the Dirac point of the Hg_3C_2 monolayer.

Notably, the Dirac cones in the Zn_3C_2 and Cd_3C_2 monolayers are robust against SOC. The SOC in these two materials is small and only produces very small gaps of 1.2 and 4.7 meV in the cones (Table 1), respectively, resulting in the large linear dispersion and existence of Dirac cones. In the vicinity of the Dirac points, the Fermi velocity (ν_f) values were calculated using the expression $\nu_f = \partial E/(\hbar\partial k)$. The ν_f values of the Zn_3C_2 monolayer along the $\Gamma \rightarrow K$ and $K \rightarrow M$ directions are 3.17×10^5 m s^{-1} and 2.73×10^5 m s^{-1}, respectively. The Fermi velocity values of the Cd_3C_2 monolayer are 3.07×10^5 and 2.65×10^5 m s^{-1} along the same two directions. These values are comparable to that in graphene (8.2×10^5 m s^{-1}).[46] To benchmark our computations, the Fermi velocity of graphene calculated using our methodology is 9.52×10^5 m s^{-1} and 7.43×10^5 m s^{-1} along the $\Gamma \rightarrow K$ and $K \rightarrow M$ directions, respectively, which are in good agreement with the previous results.[46]

It should be mentioned that previous studies suggested an intrinsic QSH insulating feature in graphene with Dirac states. Since the Hg_3C_2 monolayer has a larger SOC gap, we first checked the existence of a nonzero topological invariant,[73,74] which is a remarkable feature of QSH materials. This was directly calculated from the parities of occupied bands at time reversal invariant momenta (TRIM) due to the presence of inversion symmetry. The detailed parities of occupied bands for the M_3C_2 monolayer are listed in Fig. S4 (ESI†). The parity products for the occupied states at the TRIM of the Γ and M points were calculated to be +1 and −1, respectively. This yields a nontrivial topological invariant $\nu = 1$, which indicates the presence of the QSH effect in the M_3C_2 monolayer.

For 2D QSH insulators, the nontrivial topological feature appears due to the topological edge states connecting the VB and CB of each system at certain k-points, which is protected from back scattering. The obtained edge states are shown in Fig. 4. It can be seen that the topologically protected edge states with isotropy actually exist within the bulk band gap of the Hg_3C_2 monolayer. Due to the nontrivial topology, the edge states are robust and cut the Fermi level an odd number of times, further supporting the QSH effect in the Hg_3C_2 monolayer.

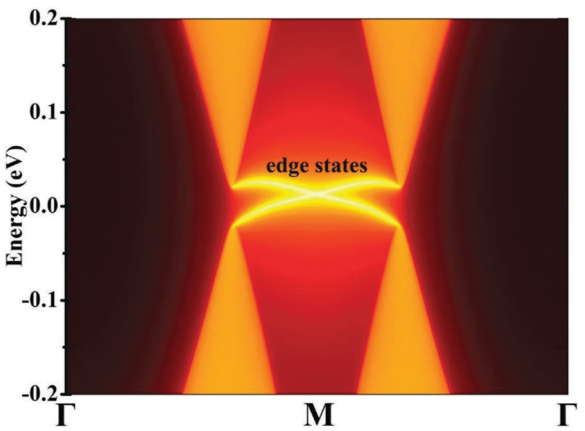

Fig. 4 Calculated topological edge states of Hg_3C_2 monolayers with the Fermi level set to zero. The edge states connect the bulk valence and conduction bands.

It is well known that nontrivial topological features are closely associated with orbital interactions. The evolution of orbitals for Hg_3C_2 at the K point is shown in Fig. 5a. With an increase in strain from −8% to −6%, the σ bond ($p_{x,y}$ d_{xy,x^2-y^2} orbitals) with parity $p = -1$ as the CB minimum is downshifted, crossing the Fermi level and finally locates below the VB maximum, which produces band inversion. Such band crossing induces a new topological node-line phase in the Hg_3C_2 monolayer (Fig. 5b), where the band gaps open when SOC is included (Fig. S5, ESI†). Such feature of 2D node-line is analogous to that in Honeycomb–Kagome Hg_3As_2[75] and different from T-graphene[76] with a closed curve band. The well-defined nontrivial Z_2 topological invariant demonstrates that the new phase also exhibits a nontrivial topological nature. Similarly, band inversion also appears in the Dirac cone materials Zn_3C_2 and Cd_3C_2 (Fig. S6, ESI†) between strains of about −8% and −6%. The nontrivial topology in the M_3C_2 monolayer mainly stems from the massive Dirac cones, which are related to the honeycomb topology with effective hopping, as illustrated for graphynes.[77,78] Although the origin of the nontrivial topology in the M_3C_2 monolayer is similar to that in graphene,[2] silicene[6,7] and BiX/SbX monolayers,[19] here the massive Dirac cones are essentially composed of the M p_z, $d_{xz,yz}$ and C p_z orbitals. This leads to new phenomena distinct from the well-known pure p-orbital Dirac cones. The SOC weakly lifts the degeneracy and opens up a fundamental gap through the Kane–Mele model, as described for graphene.[2]

Based on the above analysis, strain-induced band inversion in the Hg_3C_2 monolayer appears to drive the formation of Dirac cones (Fig. 5a). However, it is crucial to check the topological robustness against external strain. As shown in Fig. 5b for the Hg_3C_2 monolayer, upon increasing the compressive strain, the maximum of VB-1 shifts upwards and locates above the Fermi

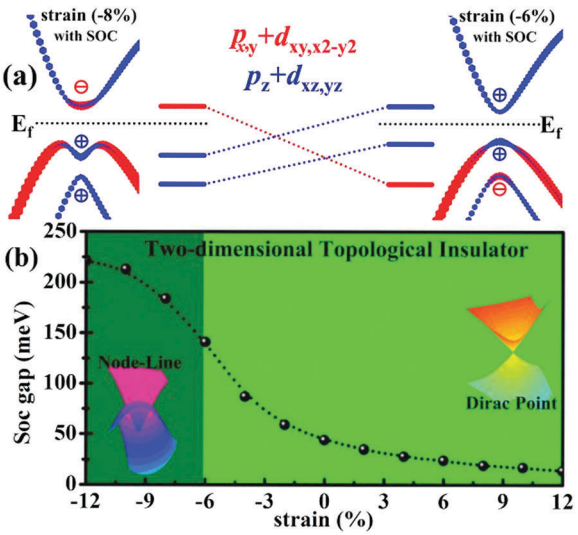

Fig. 5 (a) Schematic of the band evolution around the Fermi level at the K point with SOC. Parity values are presented near the various orbitals. (b) Nontrivial topological gap of the Hg_3C_2 monolayer as a function of applied external biaxial strain obtained with the PBE + SOC technique. Olive region: node-line semimetal phase without SOC and green region: single Dirac core phase without SOC.

level as the minimum of the CB. This causes Hg_3C_2 to be a 2D node-line semi-metal when the lattice is compressed in the range of −12 to −6% in the absence of SOC. The unchanged nontrivial topological invariant $\nu = 1$ is observed in the range from −12% to 12%, which means that Hg_3C_2 is a robust QSH insulator against external strain. Although the strain values considered here in the Hg_3C_2 monolayer are very challenging to achieve experimentally, they actually lie in an accessible strain range, as verified in graphene[79] and MoS_2[80] with strain limits of up to ∼15% and ∼11%, respectively, without substantial destruction of their crystal geometry. AIMD simulations explicitly demonstrate that M_3C_2 films under an in-plane biaxial tensile strain beyond 5% are thermodynamically stable and have no structural disruption or decomposition at 300 K (Fig. S7, ESI†). The phonon spectrum shows no negative frequencies (Fig. S8, ESI†), suggesting that the strained M_3C_2 monolayer under such a strain is dynamically stable. Thus, these strained M_3C_2 monolayers possessing the QSH effect are potentially accessible *via* epitaxial film growth on suitable substrates, nanoindentation, or mechanical stretch as demonstrated for graphene in previous experiments.[79] The other two M_3C_2 monolayers, when SOC is not included, feature node-line (in the range of −12% to −6%) and a single Dirac cone (in the range of −5% to 12%). Importantly, this feature of Dirac cones in the Zn_3C_2 and Cd_3C_2 monolayers is robust against both SOC and external strain in a large range. Similar topological evolutions are also found in the range of −12% to 12% for the Zn_3C_2 and Cd_3C_2 monolayers (Fig. S9, ESI†). These robust intrinsic properties greatly expand their potential applications in more demanding mechanical conditions, which motivate subsequent experimental studies.

Conclusions

In summary, our first-principles calculations predict that M_3C_2 (M = Zn, Cd and Hg) monolayers are a new family of 2D materials in a hexagonal lattice with intrinsic Dirac states. Here, the linear stable geometry (C═M═C) emerges, which is yet to be observed in other transition-metal-based 2D materials. The Dirac cones in the Zn_3C_2 and Cd_3C_2 monolayers are robust against SOC. The Hg_3C_2 monolayer is a room-temperature quantum spin Hall insulator with a sizable energy gap of 44.3 meV. The topological properties of the Hg_3C_2 monolayer are robust against mechanical deformation, which firmly places Hg_3C_2 in the realm of QSH materials. By applying in-plane strain, M_3C_2 (M = Zn and C) sheets show robust Dirac cone characteristics against external strain in the range of −5% to 12% and topological node-line semimetal features are observed within the compressive strain range of −12% to −6%. Overall our findings suggest a new design for possible functional materials and facilitate experimental realizations.

Conflicts of interest

There are no conflicts to declare.

Acknowledgements

This research was supported by the National Natural Science Foundation of China under Projects (21171168, 21225104, 21233009, 21301175, 21571020 and 91422303), the Natural Science Foundation of Fujian Province (2015J01071). The supports of the Supercomputer Centre of Fujian Institute of Research on the Structure of Matter (FJIRSM) are acknowledged. The work at Los Alamos National Laboratory (LANL) was supported by LANL LDRD program and was partially performed at the Center for Nonlinear Studies and at the Center for Integrated Nanotechnologies, a U.S. Department of Energy, Office of Science user facility. We also thank Dr Quansheng Wu at ETH Zürich for help with WannierTools.

References

1 K. S. Novoselov, A. K. Geim, S. V. Morozov, D. Jiang, Y. Zhang, S. V. Dubonos, I. V. Grigorieva and A. A. Firsov, *Science*, 2004, **306**, 666–669.
2 C. L. Kane and E. J. Mele, *Phys. Rev. Lett.*, 2005, **95**, 226801.
3 K. S. Novoselov, A. K. Geim, S. V. Morozov, D. Jiang, M. I. Katsnelson, I. V. Grigorieva, S. V. Dubonos and A. A. Firsov, *Nature*, 2005, **438**, 197–200.
4 A. H. C. CastroNeto, F. Guinea, N. M. R. Peres, K. S. Novoselov and A. K. Geim, *Rev. Mod. Phys.*, 2009, **81**, 109–162.
5 B. Radisavljevic, A. J. Radenovic, J. Brivio, I. Giacometti and A. Kis, *Nat. Nanotechnol.*, 2011, **6**, 147–150.
6 P. Vogt, P. De Padova, C. Quaresima, J. Avila, E. Frantzeskakis, M. C. Asensio, A. Resta, B. Ealet and G. Le Lay, *Phys. Rev. Lett.*, 2012, **108**, 155501.
7 A. Fleurence, R. Friedlein, T. Ozaki, H. Kawai, Y. Wang and Y. Yamada Takamura, *Phys. Rev. Lett.*, 2012, **108**, 245501.
8 L. F. Li, S. Z. Lu, J. B. Pan, Z. H. Qin, Y. Q. Wang, Y. L. Wang, G. Y. Cao, S. X. Du and H. J. Gao, *Adv. Mater.*, 2014, **26**, 4820–4824.
9 F. F. Zhu, W. J. Chen, Y. Xu, C. L. Gao, D. D. Guan, C. H. Liu, D. Qian, S. C. Zhang and J. F. Jia, *Nat. Mater.*, 2015, **14**, 1020–1025.
10 H. J. Zhang, C. X. Liu, X. L. Qi, X. Dai, Z. Fang and S. C. Zhang, *Nat. Phys.*, 2009, **5**, 438–442.
11 Z. G. Song, C. C. Liu, J. B. Yang, J. Z. Han, M. Ye, B. T. Fu, Y. C. Yang, Q. Niu, J. Lu and Y. G. Yao, *Nano Lett.*, 2014, **14**, 2505–2508.
12 Y. D. Ma, Y. Dai, L. Kou, T. Frauenheim and T. Heine, *Nano Lett.*, 2015, **15**, 1083–1089.
13 Y. D. Ma, Y. Dai, W. Wei, B. B. Huang and M. Whangbo, *Sci. Rep.*, 2014, **4**, 7297.
14 Y. D. Ma, L. Kou, A. Du and T. Heine, *Nano Res.*, 2014, **8**, 3412–3420.
15 C. Si, J. Liu, Y. Xu, J. Wu, B. Gu and W. Duan, *Phys. Rev. B: Condens. Matter Mater. Phys.*, 2014, **89**, 115429.
16 Y. Xu, B. H. Yan, H. J. Zhang, J. Wang, G. Xu, P. Z. Tang, W. H. Duan and S. C. Zhang, *Phys. Rev. Lett.*, 2013, **111**, 136804.

17 W. Luo and H. J. Xiang, *Nano Lett.*, 2015, **15**, 3230–3235.
18 J. J. Zhou, W. Feng, C. C. Liu, S. Guan and Y. G. Yao, *Nano Lett.*, 2014, **14**, 4767–4771.
19 Z. Song, C. C. Liu, J. Yang, J. Han, M. Ye, B. Fu, Y. Yang, Q. Niu, J. Lu and Y. Yao, *NPG Asia Mater.*, 2014, **6**, e147.
20 L. Y. Li, X. M. Zhang, X. Chen and M. W. Zhao, *Nano Lett.*, 2015, **15**, 1296–1301.
21 M. Konig, S. Wiedmann, C. Brne, A. Roth, H. Buhmann, L. W. Molenkamp, X. L. Qi and S. C. Zhang, *Science*, 2007, **318**, 766–770.
22 I. Knez, R. R. Du and G. Sullivan, *Phys. Rev. Lett.*, 2011, **107**, 136603.
23 L. Zhou, B. Shao, W. Shi, Y. Sun, C. Felser, B. Yan and T. Frauenheim, *2D Mater.*, 2016, **3**, 035022.
24 H. Weng, X. Dai and Z. Fang, *Phys. Rev. X*, 2014, **4**, 011002.
25 L. Zhou, L. Kou, Y. Sun, C. Felser, F. Hu, G. Shan, S. C. Smith, B. Yan and T. Frauenheim, *Nano Lett.*, 2015, **15**, 7867–7872.
26 L. Zhou, W. Shi, Y. Sun, B. Shao, C. Felser, B. Yan and T. Frauenheim, *2D Mater.*, 2016, **3**, 035018.
27 C. Si, K. H. Jin, J. Zhou, Z. Sun and F. Liu, *Nano Lett.*, 2016, **16**, 6584–6591.
28 M. Khazaei, A. Ranjbar, M. Arai and S. Yunoki, *Phys. Rev. B*, 2016, **94**, 125152.
29 X. Li, Y. Dai, Y. Ma, Q. Sun, W. Wei and B. Huang, *Carbon*, 2016, **109**, 788–794.
30 Y. Ma, L. Kou, Y. Dai and T. Heine, *Phys. Rev. B*, 2016, **93**, 235451.
31 S. S. Li, W. X. Ji, C. W. Zhang, P. Li and P. J. Wang, *J. Mater. Chem. C*, 2016, **4**, 2243–2251.
32 X. F. Qian, J. W. Liu, L. Fu and J. Li, *Science*, 2014, **346**, 1344–1347.
33 D. H. Choe, H. J. Sung and K. J. Chang, *Phys. Rev. B*, 2016, **93**, 125109.
34 Y. Ma, L. Kou, X. Li, Y. Dai, S. C. Smith and T. Heine, *Phys. Rev. B: Condens. Matter Mater. Phys.*, 2015, **92**, 085427.
35 Y. Sun, C. Felser and B. Yan, *Phys. Rev. B: Condens. Matter Mater. Phys.*, 2015, **92**, 165421.
36 S. M. Nie, Z. Song, H. Weng and Z. Fang, *Phys. Rev. B: Condens. Matter Mater. Phys.*, 2015, **91**, 235434.
37 W. Li, M. Guo, G. Zhang and Y. W. Zhang, *Phys. Rev. B: Condens. Matter Mater. Phys.*, 2014, **89**, 205402.
38 Y. Ma, L. Kou, X. Li, Y. Dai and T. Heine, *Phys. Rev. B*, 2016, **93**, 035442.
39 P. F. Liu, L. Zhou, T. Frauenheimc and L. M. Wu, *Nanoscale*, 2016, **8**, 4915–4921.
40 F. Ma, G. Gao, Y. Jiao, Y. Gu, A. Bilic, H. Zhang and A. Du, *Nanoscale*, 2016, **8**, 4969–4975.
41 A. Wang, Z. Wang, A. Du and M. Zhao, *Phys. Chem. Chem. Phys.*, 2016, **18**, 22154–22159.
42 P. F. Liu, L. Zhou, T. Frauenheimc and L. M. Wu, *Nanoscale*, 2017, **9**, 1007–1013.
43 X. B. Li, W. K. Huang, Y. Y. Lv, K. W. Zhang, C. L. Yang, B. B. Zhang and L. Sheng, *Phys. Rev. Lett.*, 2016, **116**, 176803.
44 R. Wu, J. Z. Ma, S. M. Nie, L. X. Zhao, X. Huang, J. X. Yin and X. Dai, *Phys. Rev. X*, 2016, **6**, 021017.
45 J. Wang, S. Deng, Z. Liu and Z. Liu, *Natl. Sci. Rev.*, 2015, **2**, 22–39.
46 D. Malko, C. Neiss, F. Viñes and A. Görling, *Phys. Rev. Lett.*, 2012, **108**, 086804.
47 M. Zhao, W. Dong and A. Wang, *Sci. Rep.*, 2013, **3**, 3532.
48 L. Z. Zhang, Z. F. Wang, B. Huang, B. Cui, Z. Wang, S. X. Du and F. Liu, *Nano Lett.*, 2016, **16**, 2072–2075.
49 Z. F. Wang, Z. Liu and F. Liu, *Phys. Rev. Lett.*, 2013, **110**, 196801.
50 Z. Liu, Z. F. Wang, J. W. Mei, Y. S. Wu and F. Liu, *Phys. Rev. Lett.*, 2013, **110**, 106804.
51 Y. Wang, J. Lv, L. Zhu and Y. Ma, *Phys. Rev. B: Condens. Matter Mater. Phys.*, 2010, **82**, 094116.
52 G. Kresse and J. Furthmüller, *Phys. Rev. B: Condens. Matter Mater. Phys.*, 1996, **54**, 11169.
53 G. Kresse and D. Joubert, *Phys. Rev. B: Condens. Matter Mater. Phys.*, 1999, **59**, 1758–1775.
54 P. E. Blöchl, *Phys. Rev. B: Condens. Matter Mater. Phys.*, 1994, **50**, 17953–17979.
55 S. Baroni, S. D. Gironcoli, A. D. Corso and P. Giannozzi, *Rev. Mod. Phys.*, 2001, **73**, 515–562.
56 A. Togo, F. Oba and I. Tanaka, *Phys. Rev. B: Condens. Matter Mater. Phys.*, 2008, **78**, 134106.
57 S. Nosé, *J. Chem. Phys.*, 1984, **81**, 511–519.
58 M. L. Sancho, J. L. Sancho, J. L. Sancho and J. Rubio, *J. Phys. F: Met. Phys.*, 1985, **15**, 851.
59 A. A. Mostofi, J. R. Yates, Y. S. Lee, I. Souza, D. Vanderbilt and N. Marzari, *Comput. Phys. Commun.*, 2008, **178**, 685–699.
60 Q. Wu, S. Zhang, H. F. Song, M. Troyer and A. A. Soluyanov, WannierTools: An open source software package for novel topological materials. *arXiv preprint*, 2017, arXiv:1703.07789.
61 P. F. Liu, L. Zhou, T. Frauenheim and L. M. Wu, *Phys. Chem. Chem. Phys.*, 2016, **18**, 30379–30384.
62 X. Wang, A. M. Jones, K. L. Seyler, V. Tran, Y. Jia, H. Zhao and F. Xia, *Nat. Nanotechnol.*, 2015, **10**, 517–521.
63 L. Li, Y. Yu, G. J. Ye, Q. Ge, X. Ou, H. Wu and Y. Zhang, *Nat. Nanotechnol.*, 2014, **9**, 372–377.
64 S. Zhang, M. Xie, F. Li, Z. Yan, Y. Li, E. Kan and H. Zeng, *Angew. Chem.*, 2016, **128**, 1698–1701.
65 M. Pumera and Z. Sofer, *Adv. Mater.*, 2017, 1605299.
66 M. Zhou, W. Ming, Z. Liu, Z. Wang, P. Li and F. Liu, *Proc. Natl. Acad. Sci. U. S. A.*, 2014, **111**, 14378–14381.
67 R. C. Andrew, R. E. Mapasha, A. M. Ukpong and N. Chetty, *Phys. Rev. B: Condens. Matter Mater. Phys.*, 2012, **85**, 125428.
68 F. Mouhat and F. X. Coudert, *Phys. Rev. B: Condens. Matter Mater. Phys.*, 2014, **90**, 224104.
69 J. Heyd, G. E. Scuseria and M. Ernzerhof, *J. Chem. Phys.*, 2003, **118**, 8207–8215.
70 J. Heyd, G. E. Scuseria and M. Ernzerhof, *J. Chem. Phys.*, 2006, **124**, 219906.
71 M. A. Omary, T. R. Webb, Z. Assefa, G. E. Shankle and H. H. Patterson, *Inorg. Chem.*, 1998, **37**, 1380–1386.
72 A. Savin, R. Nesper, S. Wengert and T. F. Fässler, *Angew. Chem., Int. Ed. Engl.*, 1997, **36**, 1808–1832.
73 L. Fu and C. L. Kane, *Phys. Rev. B: Condens. Matter Mater. Phys.*, 2007, **76**, 045302.
74 L. Fu, C. L. Kane and E. J. Mele, *Phys. Rev. Lett.*, 2007, **98**, 106803.

75 J. L. Lu, W. Luo, X. Y. Li, S. Q. Yang, J. X. Cao, X. G. Gong and H. J. Xiang, *Chin. Phys. Lett.*, 2017, **34**, 057302.
76 H. Huang, Y. Li, Z. Liu, J. Wu and W. Duan, *Phys. Rev. Lett.*, 2013, **110**, 029603.
77 X. Qin, Y. Liu, B. Chi, X. Zhao and X. Li, *Nanoscale*, 2016, **8**, 15223–15232.
78 H. Huang, W. Duan and Z. Liu, *New J. Phys.*, 2013, **15**, 023004.
79 C. Lee, X. Wei, J. W. Kysar and J. Hone, *Science*, 2008, **321**, 385–388.
80 S. Bertolazzi, J. Brivio and A. Kis, *ACS Nano*, 2011, **5**, 9703–9709.